CrossMark

Investigation of structural, morphological, optical and electrical properties of double-doping Lanthanum ferrite

F. B. Abdallah[1] · A. Benali[1] · M. Triki[1] · E. Dhahri[1] · K. Nomenyo[2] · G. Lerondel[2]

Abstract

Polycrystalline compounds of $La_{0.75}Ba_{0.25-x}Sr_xFeO_3$ containing different amounts of Sr (x = 0.00, 0.05, 0.10 and 0.15) were synthesized by the sol–gel method. The samples were characterized by means of X-ray diffraction (XRD), scanning electron microscope (SEM), FTIR and Raman spectroscopy, UV–Vis spectroscopy and I–V electrical measurements. XRD analysis reveals that all samples possess an orthorhombic structure with *Pnma* space group. The Lattice parameter values are found to decrease with the increase of Sr contents. The surface morphology and microstructure were analyzed using SEM images. It is found that all samples have similar microstructure morphology, but differ in the range of grain sizes. Raman spectroscopy measurements exhibit slight shift in Raman modes with Sr-doping. A shift of characteristic peaks for Fe–O bond in FTIR spectra were observed with the increase of Sr content. Using the Tauc plot methodology, the optical band gap values have been evaluated from the UV–Vis measurements. These values increase with Sr content. Finally, room temperature electrical resistivity decreases with Sr content increasing. The obtained results show that the structural, optical and electrical properties have low strongly affected by the strontium content.

1 Introduction

Over the past few decades, lanthanum orthoferrite with the chemical formula $LaFeO_3$ have of great interest owing to their technical importance and the fundamental interest in physical and chemical properties [1]. These interesting properties allow the material to be used in novel applications in the field of science and technology [2–6].

$LaFeO_3$ is an orthorhombically distorted perovskite crystal structure with the strong super exchange interactions between the Fe^{3+}–Fe^{3+} through O^{2-} ion leading to the antiferromagnetic state above $T_N = 740$ K. It has a structural transition from *Pnma* to R$\bar{3}$c at 1228 K as well as a subsequent transition to Pm3m at 2140 K [7, 8]. The La site doping with other transition metal ions is believed to be an effective way to alter the properties. In this regard, a variety of doped $LaFeO_3$ have been reported where doping affects the structural properties and improves its physico-chemical properties [9–12]. For instance, Jones et al. [13] indicated that Sr doping of $LaFeO_3$ should enhance oxide–ion conductivity because of the low binding energy of dopant–oxygen vacancy clusters and the increase in vacancy concentration. The role of Sr doping on the structure and microstructural properties of $LaFeO_3$ was studied by Jain et al. [14]. An increase in lattice parameters and decreases in X-ray density were observed with an increase in doping concentration. Wu et al. [15] investigated the magnetization behavior of a series Sr doped $La_{1-x}Sr_xFeO_3$ compounds. They found that the Sr^{2+} dopant affect the stability of the robust antiferromagnetic coupling between Fe ions and induce new phase transitions paramagnetic (PM) to ferromagnetic (FM) at about 300 K. On the other hand, Sun et al. [16] demonstrated that the substitution of the lanthanum atoms in the $LaFeO_3$ compound by Ba^{2+} could reduce the resistance and improve the sensing response. The optical properties have attracted attention for doped $LaFeO_3$. Karthikeyan et al. [17] focused on the Ba and Ca doped $LaFeO_3$ perovskite. They found that the optical gap to be 2.21 eV and 2.27 eV for $La_{0.9}Ba_{0.1}FeO_3$ and $La_{0.9}Ca_{0.1}FeO_3$ compounds. Compared with energy gap values of the $LaFeO_3$ is 2.52 eV, the decreasing is ascribed to the subsistence of impurities by the dopant atoms, local

✉ F. B. Abdallah
fatmaabdallahphysique@gmail.com

[1] Laboratoire de Physique Appliquée, Faculté des Sciences de Sfax, Université de Sfax, B.P. 1171, 3000 Sfax, Tunisia

[2] Lumière, nanomatériaux et nanotechnologie (L2n), Institut Charles Delaunay, CNRS UMR 6281, Université de Technologie de Troyes, 12 rue Marie Curie, BP 2060, 10010 Troyes, France

distortions and oxygen vacancy which leads to inducement of additional electronic levels in the forbidden band levels.

Much work has been done in the past to study the effects of substitution in the La site of $LaFeO_3$, but not much work has been done to report the effect of double doping at the La site. In our group, Benali et al. found that Ca–Pb double doping at the La site in $LaFeO_3$, can lead to the resistivity modification and sensitivity improvement to ethanol gas. They also found the substitution of calcium by lead introduces a change on the magnitude of the magnetization curves. This behavior was related to the competing mechanisms between the Fe^{3+}–Fe^{3+} tetrahedral FM interactions and the octahedral antiferromagnetic ones between Fe^{3+} and Fe^{2+} ions [9, 18].

In general, pure and doped $LaFeO_3$ properties depend not only on their composition but also on the structure, morphology, phase and size, which are strongly related to the preparation method. So that the improvement of the method of preparation is the subject of much attention on the part of the researchers [19]. Until now, several methods have been reported for the synthesis of $LaFeO_3$, including ceramic solid state reaction [20], sol–gel [21, 22], spray drying and co-precipitation [23, 24]. Among these, the sol gel process has proved to be one of the most successful methods, it is an ideal technique for synthesizing $LaFeO_3$ perovskite with high purity, controlled stoichiometry, narrow particle size distribution and controlled morphology.

Sr and Ba doped $LaFeO_3$ are known for their good electrical conductivities and electrocatalytic activities. Then, we selected the Sr and Ba as co-doping in $LaFeO_3$ to improve the properties of samples and to enhance its applications in gas sensor and visible light photocatalytic activity.

Based on the facts described above, the aim of his work is to study the strontium doping effects on the structural, morphological, optical and electrical properties of $LaFeO_3$ doped barium, prepared using sol gel method. To the best of our knowledge, no systematic study about the physical properties of Sr doped $La_{0.75}Ba_{0.25-x}Sr_xFeO_3$ compounds has yet been reported.

2 Experimental details

2.1 Samples preparation

$La_{0.75}Ba_{0.25-x}Sr_xFeO_3$ samples (x = 0.00, 0.05, 0.10, 0.15) were prepared by the sol–gel method, using metal nitrates as precursors [25]. All chemicals used here were of analytical grade without any further purification. Stoichiometric amounts of $La(NO_3)_3 \cdot 6H_2O$, $Sr(NO_3)_2$, $Ba(NO_3)_2$ and $Fe(NO_3)_3 \cdot 9H_2O$ were firstly dissolved in distilled water. Then, citric acid was added to the solution in the mole ratio 2:1 with respect to the total amount of cations, followed by the addition of the ethylene glycol as a polymerization

agent. The solution was then heated at 70 °C until a wet gel of the metal nitrates was obtained. Prepared gels were dried, ground in agate mortar and then heated in air at 300 °C for 12 h to produce powdered samples. Finally, the samples were pressed into pellets (of about 1 mm thickness and 8 mm diameter) and sintered respectively at 600 °C (24 h), 800 °C (24 h) and 900 °C (24 h) in order to obtain the crystalline phase.

2.2 Characterization techniques

The structure and phase purity of the obtained $La_{0.75}Ba_{0.25-x}Sr_xFeO_3$ (x = 0.00, 0.05, 0.10 and 0.15) samples were checked out by X-ray diffraction (XRD) measurements made at room temperature with an INEL Equinox 100 diffractometer using Cu Kα X-ray source radiation (1.5406 Å).

Morphological analysis was studied by a scanning electron microscope (SEM) (Hitachi SU8030). The chemical composition was determined with an EDX analyzer attached with a Hitachi SU8030 instrument.

The Fourier transform infrared (FTIR) spectra were recorded in the wavenumber range of 4000–400 cm^{-1} using a Perkin Elmer spectrometer. A Horiba-JobinYvon spectrometer was employed to record the Raman spectra, using the 632.8 nm radiation of a HeNe laser.

UV–Vis measurements were performed using a Varian Cary 300 spectrophotometer in glass cuvette with a path length of 1 cm over the wavelength range of 300–850 nm.

The electrical measurements of the samples were obtained by four-point probe technique. A Keithley 2634B sourcemeter was used to provide the constant current and the potential drop was measured by a Keithley 2700 multimeter through interface card, controlled by a computer.

3 Results and discussion

3.1 Structural and morphology analysis

Room temperature X-ray powder diffraction patterns for $La_{0.75}Ba_{0.25-x}Sr_xFeO_3$ samples (x = 0.00, 0.05, 0.10 and 0.15) are represented in Fig. 1a and indicate that all samples have the same perovskite structure. The Rietveld analysis using the FullProf software [26] have been carried out for an orthorhombic structure with the *Pnma* space group. It can be observed that the lattice parameters and the cell volume decrease with the increase of strontium content, due to the smaller ionic radius of Sr^{2+} (1.31 Å) compared to Ba^{2+} ions (1.47 Å) [27]. This evolution of the cell parameters is also confirmed by the shift of the most intense peak (121) for all samples to higher angles as marked in Fig. 1b. This shifting is because of the structural
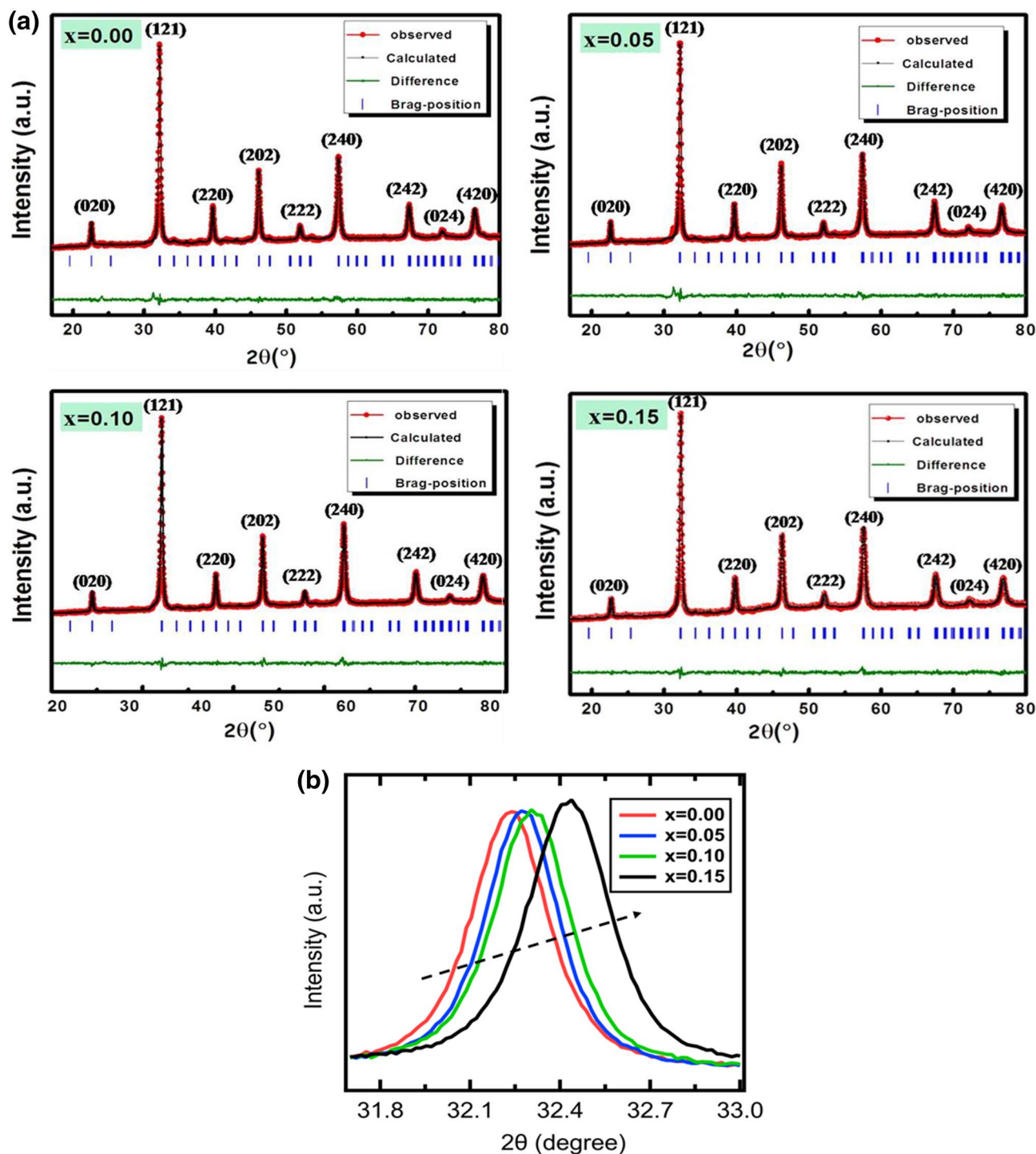
Fig. 1 **a** Room temperature Rietveld refined powder XRD pattern of $La_{0.75}Ba_{0.25-x}Sr_xFeO_3$ (x = 0.00, 0.05, 0.10 and 0.15). **b** The variation in the most intense peak of $La_{0.75}Ba_{0.25-x}Sr_xFeO_3$ (x = 0.00, 0.05, 0.10 and 0.15)

distortion taking place due to doping and it is more marked for the compound x = 0.15. Detailed refinement parameters are listed in Table 1 and their variation versus the strontium concentration are shown in Fig. 2.

To estimate the average crystallite size values of the prepared powders, Scherrer and Williamson–Hall methods were used.

The Scherrer formula can be described as follows [25]:

Table 1 Cell parameters, X-ray density (d_x) and porosity values of $La_{0.75}Ba_{0.25-x}Sr_xFeO_3$ (x = 0.00, 0.05, 0.10 and 0.15)

x	0.00	0.05	0.10	0.15
Space group	*Pnma*	*Pnma*	*Pnma*	*Pnma*
a (Å)	5.559	5.551	5.544	5.539
$b/\sqrt{2}$ (Å)	5.562	5.557	5.550	5.545
c (Å)	5.568	5.563	5.560	5.552
V (Å^3)	60.894	60.688	60.455	60.307
d_x (g/cm^3)	2.343	2.329	2.313	2.295
Porosity (%)	53.68	53.36	53.05	52.67
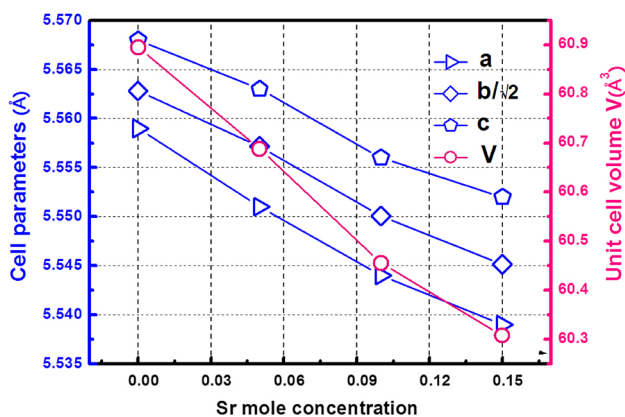
Fig. 2 Lattice parameter and volume plot of $La_{0.75}Ba_{0.25-x}Sr_xFeO_3$ (x = 0.00, 0.05, 0.10 and 0.15)

Table 2 Average crystallite size and average grain size values of $La_{0.75}Ba_{0.25-x}Sr_xFeO_3$ (x = 0.00, 0.05, 0.10 and 0.15)

Compounds	Average crystallite size		Average grain size (nm)
	Scherer's method D_s (nm)	W–H method D_W (nm)	SEM D_{SEM} (nm)
$La_{0.75}Ba_{0.25}FeO_3$	24	43	35
$La_{0.75}Ba_{0.2}Sr_{0.05}FeO_3$	27	60	50
$La_{0.75}Ba_{0.15}Sr_{0.1}FeO_3$	25	57	40
$La_{0.75}Ba_{0.1}Sr_{0.15}FeO_3$	23	35	55

$$D_S = \frac{k \times \lambda}{\beta \cos(\theta)} \qquad (1)$$

where D_S is the average crystallite size, k is the shape factor, λ represents the X-ray wavelength (1.5405 Å for CuK$_\alpha$ radiation), β is full width at half maximum and θ is the Bragg diffraction angle of the most intense peak. The values of D_S are shown in Table 2.

According to Williamson–Hall method, the individual contributions to the line broadening of a Bragg reflection can be defined as follows [28]:

$$\beta \times \cos(\theta) = \frac{K \times \lambda}{D_w} + [4 \times \varepsilon \times \sin(\theta)] \qquad (2)$$

where D_W is the average crystallite size and ε is the effective strain. Equation 2 represents a straight line between 4sin θ (x-axis) and β cos θ (y-axis) (Fig. 3). The strain is calculated from the slope of the line and the average crystallite size can be determined from the intercept ($k\lambda/D_W$) of this line on the vertical axis. The values of D_W are listed in Table 2.

It is worth noting that the crystallite size determined from the Williamson–Hall method, higher than those calculated using Scherer's formula, because the broadening effect due to strain is completely excluded in Scherer's method [29].

X-ray density (d_x) was calculated using the following relation [30]:

$$d_x = \frac{M}{N \times a^3} \qquad (3)$$

where *M* is the molecular weight of the samples, *N* the Avogadro's number and *a* is the lattice constant. The X-ray density (d_x) values are summarized in Table 1. As clearly shown in this table, the X-ray density decrease with an increase in the Sr^{2+} content which could be attributed to its dependence on molecular weight and lattice parameter of the sample [31].

The porosity (*P*) was also calculated using the expression [18]:

$$P(\%) = 1 - \frac{d_B}{d_x} \qquad (4)$$

where d_B represent the bulk density. As mentioned in Table 1, the porosity decreases with increase in strontium concentration. This may be related to the decrease in crystallite size.

Therefore, a decrease in both molecular weight and lattice parameter with the increase of Sr concentration in $La_{0.75}Ba_{0.25-x}Sr_xFeO_3$, leads to a decrease in X-ray density and porosity.

This structural study by XRD is complemented by surface morphology analysis using SEM. As observed in Fig. 4, a non-uniform grain distribution throughout the sample occurs. In all compounds with different Sr amount, the grains are found to be irregular in the shape and size. The average grain size can be analyzed through the histogram (Fig. 4) using the Image-J software, as represented in Table 2.

For all samples, the average grain size was found to be in the range of 35 and 55 nm, which is almost of the
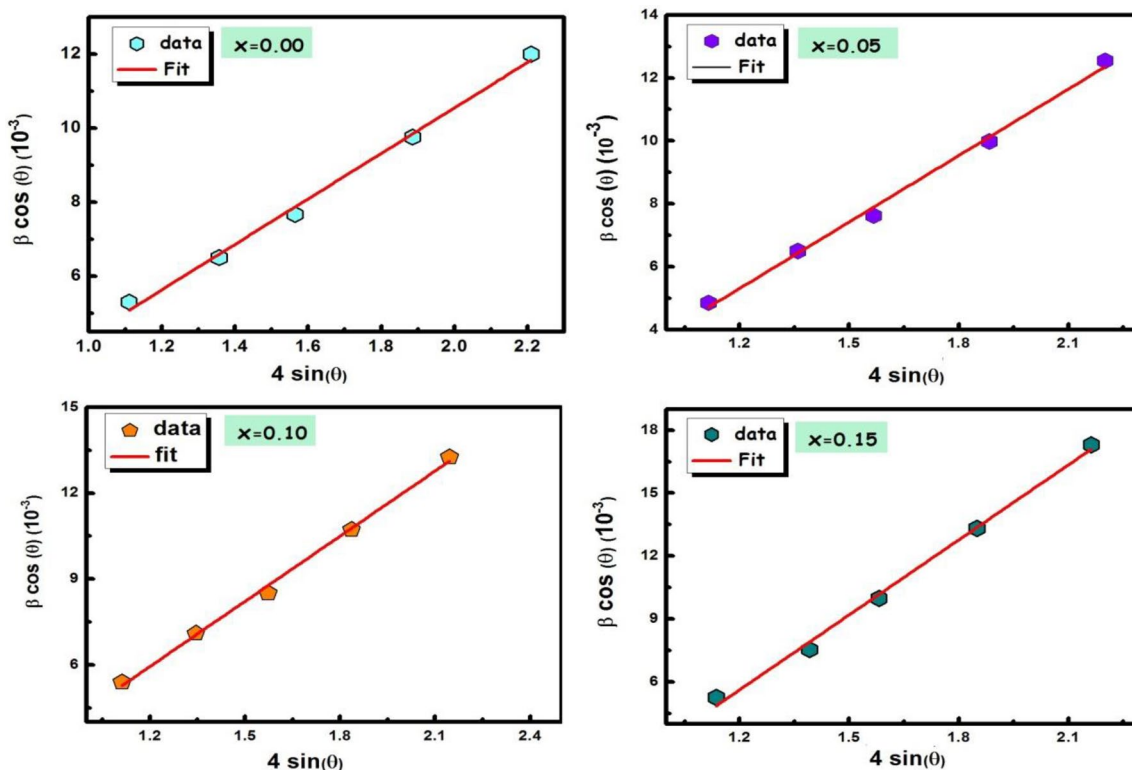
Fig. 3 Williamson–Hall plot of $La_{0.75}Ba_{0.25-x}Sr_xFeO_3$ (x = 0.00, 0.05, 0.10 and 0.15)

same order of magnitude as the average crystallite size calculated by XRD, which indicates that the grain is a single crystal.

The elemental compositions of the synthesized samples were thoroughly analyzed by the energy dispersive X-ray spectroscopy (EDS), as shown in Fig. 5. The presence of the X-ray peaks corresponding to various atoms shows the successful substitution of Sr in the $La_{0.75}Ba_{0.25-x}Sr_xFeO_3$. The elemental compositions in terms of atomic percentages and weight percentages are tabulated in the insets of Fig. 5. The elemental composition values are almost in close agreement with the stoichiometry of starting materials used for the preparation of samples.

3.2 FTIR and Raman analysis

Characteristic chemical bonding of the synthesized samples was investigated by FTIR and Raman spectroscopy. The FTIR spectra are shown in Fig. 6. A strong absorption band is present at 556 cm^{-1} assigned to Fe–O asymmetrical stretching vibration. This band indicates the formation of lanthanum orthoferrite [32]. The observed small peaks at about 850 cm^{-1} reveals the presence of metal oxide-bonds which are assigned to the vibrations of Fe–O and O–Fe–O bonds. The vibrational bands present at 1420 cm^{-1} were ascribed to C=O and C–O–C stretching vibrations for the

ester groups due to the esterification between citric acid and ethylene glycol [33–35]. It is noteworthy that all these spectra are similar in shape with a slight shift of the Fe–O absorption stretching vibration towards the shorter wavenumber. This is due to the perturbation occurring in the $Fe^{3+}–O^{2-}$ bond by replacing Sr^{2+} ions. The transmittance change produces a significant difference at x = 0.15, which may be due to the distortion of the crystalline structure when the Sr concentration level reaches 0.15. This difference is in accordance with X-ray peak shifting.

Raman spectroscopy is a very powerful tool to determine structural phase transitions and oxygen motion of perovskite-type materials [36]. This method is more surface-sensitive than XRD because its excitation energy is less penetrating than X-ray [37]. As observed from XRD analysis that the $La_{0.75}Ba_{0.25-x}Sr_xFeO_3$ has adopted the orthorhombic crystal structure with *Pnma* space group. Based in the symmetry operations of this space group carried out by Smirnova et al. there are 24 Raman active modes [38]:

$$\Gamma_{Raman}(Pnma) = 7A_g + 5B_{1g} + 7B_{2g} + 5B_{3g} \quad (5)$$

These 24 Raman modes can be classified into anti-symmetric stretching (four modes), symmetric stretching (two modes), bending (four modes), rotation/tilting of the BO_6 octahedral (six modes) and remaining eight Raman modes related to the motion of A-site cation in ABO_3. Figure 7
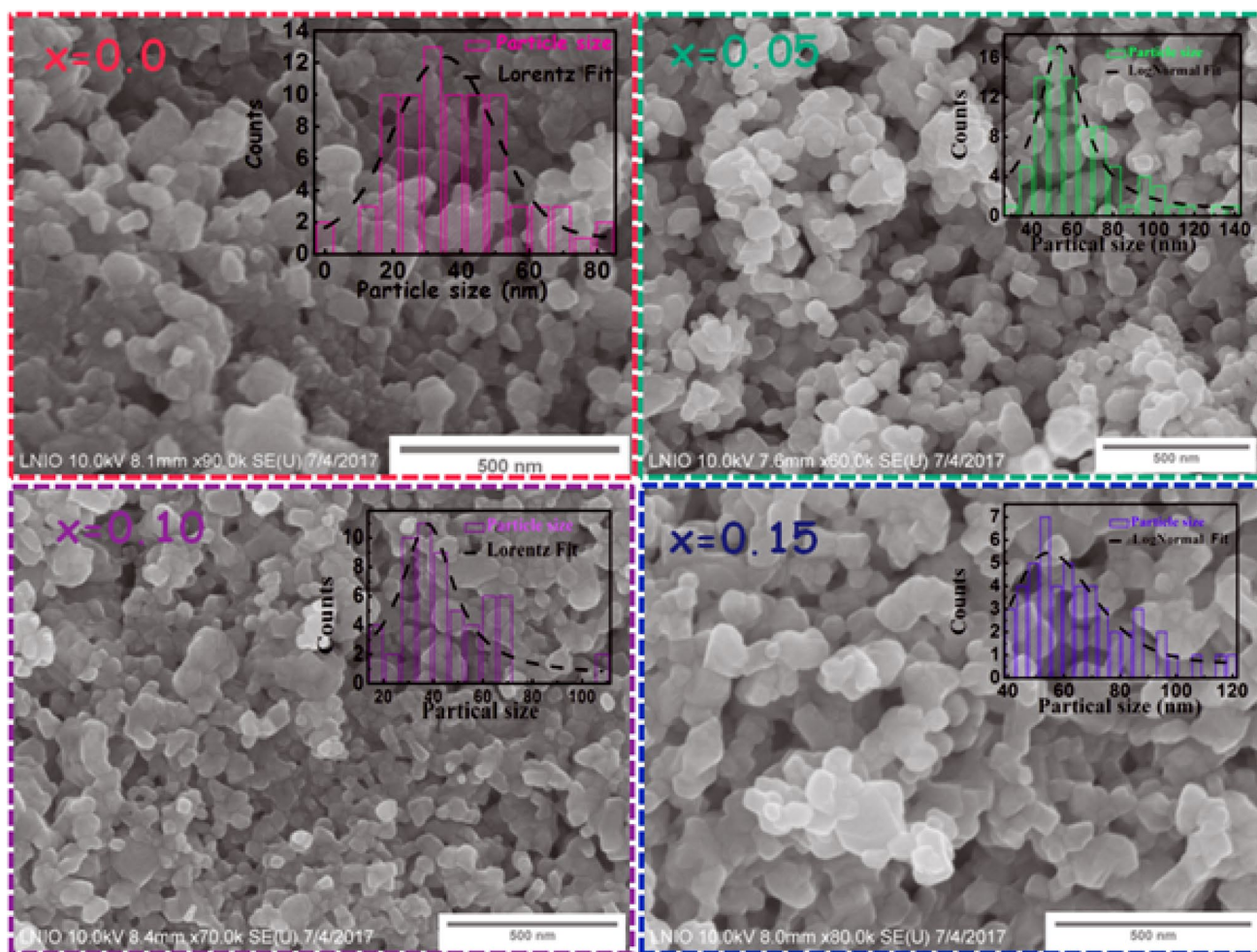
Fig. 4 SEM micrographs and corresponding histogram plot for particle size distributions of $La_{0.75}Ba_{0.25-x}Sr_xFeO_3$ ($x = 0.00$, 0.05, 0.10 and 0.15)

shows the Raman spectra for $La_{0.75}Ba_{0.25-x}Sr_xFeO_3$ with $x = 0.00$, 0.05, 0.10 and 0.15 in the wavenumber range 100–1000 cm^{-1} at room temperature. The observed spectra exhibit similar Raman vibrations, confirming the same *Pnma* symmetry [39]. All the Raman peaks were fitted using a Lorentzian functions which peak positions are indicated in Table 3. The Raman modes assigned to B_{1g} (5) are related to the Lanthanum vibrations present in the samples. The Raman mode assigned to Ag (4) is due to stretching vibrational frequencies of FeO_6 octahedra in our material [40, 41]. As already observed, with the introduction of Sr^{2+} ions, a slight frequency shift of the Raman peaks for all phonon modes has been noted. The substitution of strontium induces a decrease of the lattice parameter that is responsible for a shift of the vibrational modes. The Raman spectra shows that there is a suppression of Raman modes with Sr doping for $x = 0.15$, that may be due to the distortion and weakening of the exchange interaction. Indeed, the results from the Raman study are consistent with the XRD and FTIR studies. Further, it is well known that vibrational properties are

significantly affected due to some factors such as creation of defects, distribution of the crystallite size and phonon confinement effects [42].

3.3 Band gap energy measurement

UV–Vis spectroscopy was used to explore the optical properties of the synthesized samples. It provides simple methods for explaining some features concerning the band gap energy [43]. The optical absorption spectra for $La_{0.75}Ba_{0.25-x}Sr_xFeO_3$ samples with different Sr concentrations are shown in Fig. 8a.

The approximate values of the energy band gap (E_g) were obtained by the Tauc relationship [44, 45]:

$$\alpha h\nu = B(h\nu - E_g)^n \tag{6}$$

where α is absorption coefficient ($\alpha = 2.303 A/t$, here A is the absorbance and t is the thickness of the cuvette), h is Planck's constant, ν is the photon frequency, B is constant, E_g is the optical band gap and n is an index that characterizes
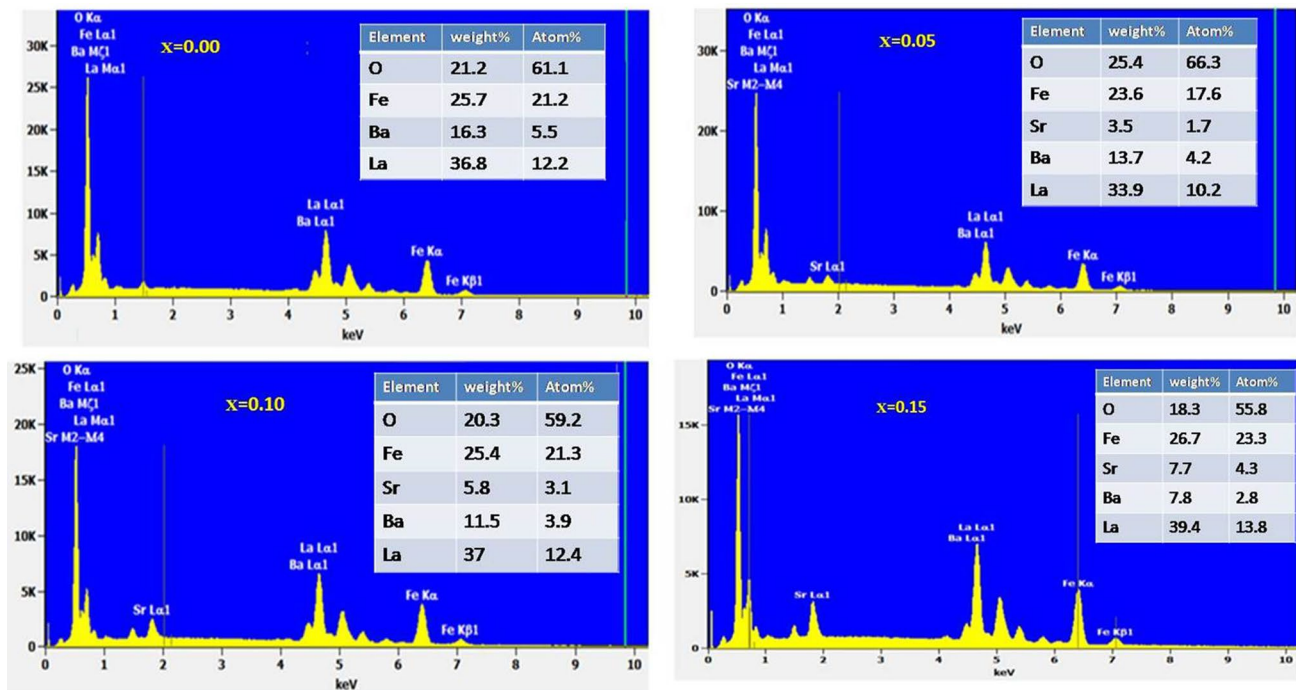
Fig. 5 EDS spectra of $La_{0.75}Ba_{0.25-x}Sr_xFeO_3$ (x = 0.00, 0.05, 0.10 and 0.15). The inset tables are the corresponding atomic ratio and weight ratio of the detected elements
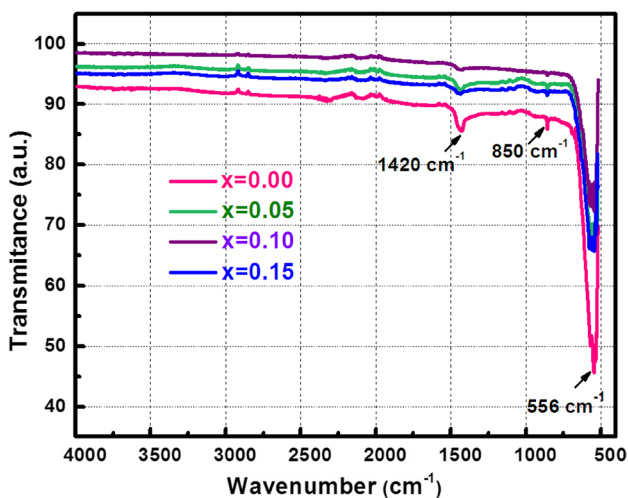
Fig. 6 FTIR spectra of $La_{0.75}Ba_{0.25-x}Sr_xFeO_3$ (x = 0.00, 0.05, 0.10 and 0.15)

the optical absorption process and it is theoretically equal to 1/2 for a direct band gap semiconductor.

An extrapolation of the linear region of plot $(\alpha h\nu)^2$ versus $h\nu$ gives the values of the optical band gap Eg, as shown in Fig. 8b. The estimated band energies of the x = 0.00, x = 0.05, x = 0.10 and x = 0.15 samples were found to be equal to 2.98, 3.09, 3.20 and 3.25 eV, respectively. Figure 8c

shows the variation of optical band gap energies with strontium amount. The observed increase in band gap values with the increase of Sr concentration could be attributed to the basis of the Burstein–Moss effect [46]. As increasing the doping concentration, the donor states are created, which pushes the Fermi level higher in energy and in the case of degenerate doping level, the Fermi level gets closer to the conduction band above the busy donor state. Only one electron can be excited from the valence band to the conduction band above the Fermi level, since all states below the Fermi level are occupied by donor states. As a consequence, an increase in the optical band gap is observed with the increase in strontium concentration [47].

Such a value of the band gap energy suggests that these compounds may be a potential candidate for new high frequency optoelectronic devices, since the materials having the band gap energy greater than 2 eV is of particular interest in the UV region of the spectrum [48, 49]. As conclusion one can say that band gap is a critical parameter from application point of view.

3.4 Current–voltage (I–V) characteristics

The last characterizations are achieved by the voltage–current measurements, in order to understand the electrical behavior of $La_{0.75}Ba_{0.25-x}Sr_xFeO_3$. Figure 9a shows the I–V characteristic curves for all samples recorded at room
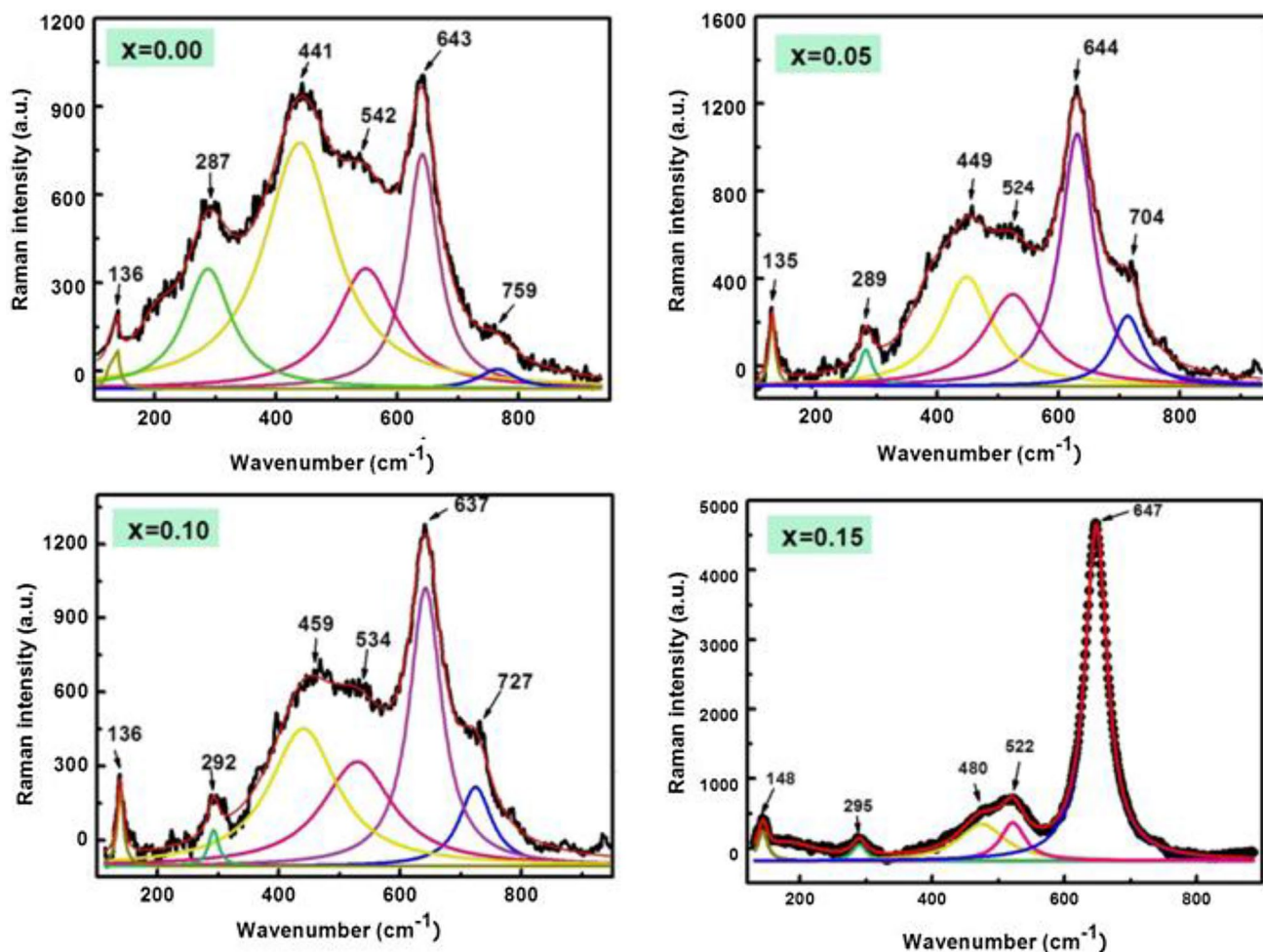
Fig. 7 Raman spectra of $La_{0.75}Ba_{0.25-x}Sr_xFeO_3$ (x = 0.00, 0.05, 0.10 and 0.15)

Table 3 Assigned Raman modes of $La_{0.75}Ba_{0.25-x}Sr_xFeO_3$ (x = 0.00, 0.05, 0.10 and 0.15)

Raman modes	x = 0.00	x = 0.05	x = 0.10	x = 0.15
$B_{1g(5)}$	136	135	136	148
$A_{g(4)}$	287	289	292	297
B_{3g}	441	449	459	480
$A_{g(3)}$	542	524	534	522
B_{1g}	643	644	647	647
	759	727	704	–

$$\rho = 2\pi S \frac{\Delta V}{\Delta I} \tag{7}$$

The typical variation of resistivity obtained from the I–V curves as a function of the Sr doping concentration is shown in Fig. 9b. It is seen that the resistivity values decrease with increasing the concentration of Sr^{2+} ions. However, when the Ba^{2+} (ionic radius = 1.47 Å) is replaced by the Sr^{2+} with smaller ionic radius (ionic radius = 1.31 Å), the charge carriers are given more mobility that enhances the conductivity and reduces the resistivity.

temperature. All I–V curves exhibit a non-ohmic electrical response. It is attributed to the formation of Schottky barriers due to a mismatch in the number of charge carriers.

The electrical resistivity of the samples was by loading a direct current through the outer pair of probes and measuring the voltage drop between the inner pair of probes which are positioned at a distance of s = 1 mm, using the following equation [50]:

4 Conclusions

In summary, the Sr-doping in $La_{0.75}Ba_{0.25-x}Sr_xFeO_3$ prepared by the sol–gel method affect the various physical properties of this system.

The lattice parameters and the unit cell volume monotonically decrease with increasing Sr^{2+} content, which can be

(a)

(b)

(c)
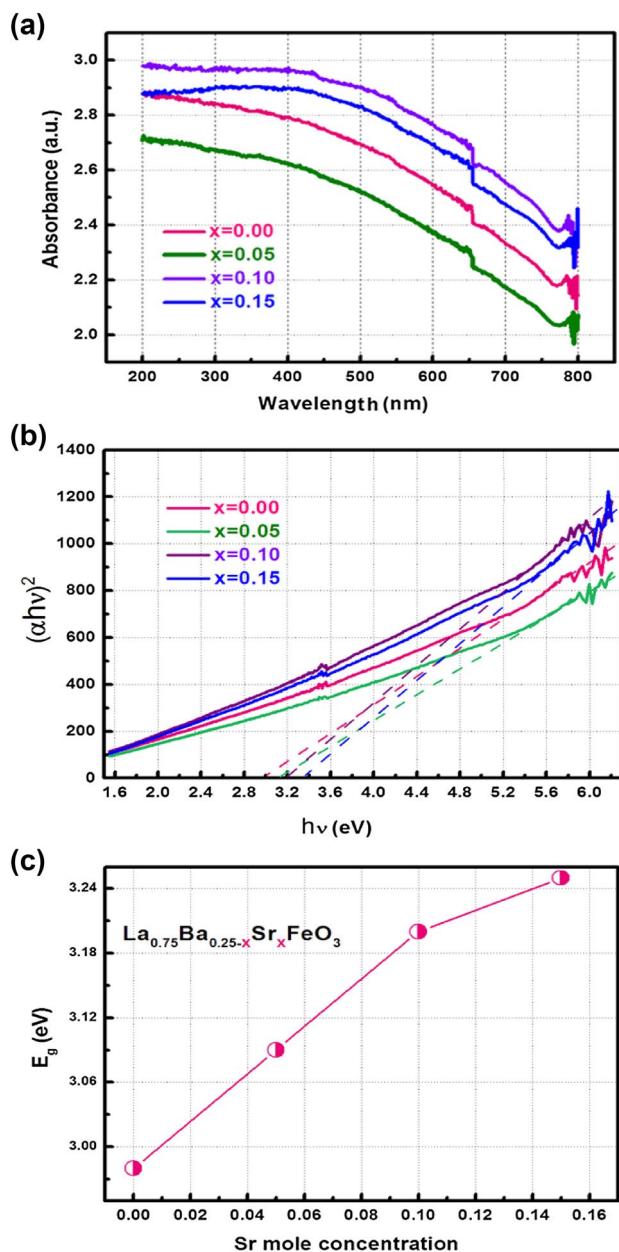
Fig. 8 **a** UV–Vis absorbance spectra of $La_{0.75}Ba_{0.25-x}Sr_xFeO_3$ (x = 0.00, 0.05, 0.10 and 0.15). **b** Plots of $(\alpha h\nu)^2$ versus photon energy ($h\nu$), and **c** energy band gap (Eg) variation with Sr concentration for all samples

attributed to a change in the A-site ionic radius. Morphology analysis revealed a non-uniform grain distribution. The introduction of strontium into $La_{0.75}Ba_{0.25-x}Sr_xFeO_3$ leads to a shift of the Raman peaks and characteristic peaks of the Fe–O bond in FTIR spectra.

The optical band gap obtained from UV–Vis results, increases with the Sr concentration. The non-ohmic nature of all samples is confirmed by I–V characteristic curves. The room temperature electrical resistivity decreases with

(a)

(b)
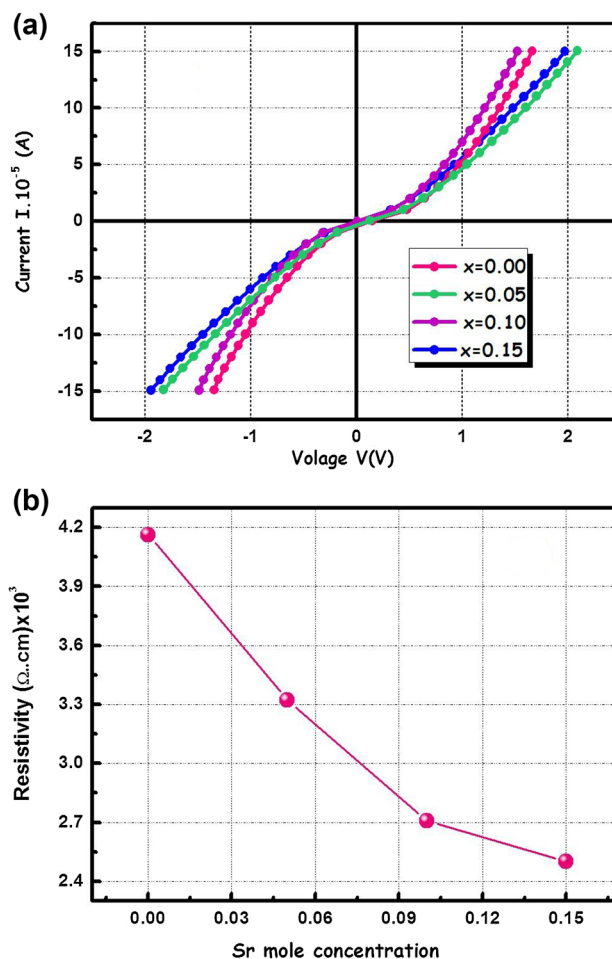
Fig. 9 **a** I–V curves of $La_{0.75}Ba_{0.25-x}Sr_xFeO_3$ (x = 0.00, 0.05, 0.10 and 0.15) recorded at room temperature. **b** Room temperature resistivity variation with Sr concentration

increasing the Sr content. Consequently, the electrical properties were enhanced with increasing Sr^{2+} ion content.

A good correlation between structural, optical and electrical properties has been observed for all the studied samples. Actually, the distortion of the structure caused by doping leads to a change in optical properties and a reduction in electrical resistivity.

References

1. C.A. Dixon, C.M. Kavanagh, K.S. Knight, W. Kockelmann, F.D. Morrison, P. Lightfoot, J. Solid State Chem. **230**, 337 (2015)
2. S.N. Tijare, M.V. Joshi, P.S. Padole, P.A. Mangrulkar, S.S. Rayalu, N.K. Labhsetwar, Int. J. Hydrog. Energy **37**, 10451 (2012)

3. K. Huang, H.Y. Lee, J.B. Goodenough, J. Electrochem. Soc. **145**, 3220 (1998)
4. G. Martinelli, M.C. Carotta, M. Ferroni, Y. Sadaoka, E. Traversa, Sens. Actuator B **55**, 99 (1999)
5. Y. Nishihata, J. Mizuki, T. Akao, H. Tanaka, M. Uenishi, M. Kimura, T. Okamoto, N. Hamada, Nature **418**, 164 (2002)
6. H. Saoudi, A. Benali, M. Bejar, E. Dhahri, T. Fiorido, K. Aguir, R. Hayn, J. Alloys Compd. **731**, 655 (2018)
7. W.C. Koehler, E.O. Wollan, J. Phys. Chem. Solids **2**, 100 (1957)
8. S.M. Selbach, J.R. Tolchard, A. Fossdal, T. Grande, J. Solid State Chem. **196**, 249 (2012)
9. A. Benali, M. Bejar, E. Dhahri, M. Sajieddine, M.P.F. Graça, M.A. Valente, Mater. Chem. Phys. **149–150**, 467 (2015)
10. A.S. Mahapatra, A. Mitra, A. Mallick, M. Ghosh, P.K. Chakrabarti, Mater. Lett. **169**, 160 (2016)
11. S. Nawaz, H. Malik, M.F. Warsi, M. Shahid, I. Shakir, A. Wadood, M.A. Khan, Ceram. Int. **41**, 6812 (2015)
12. K. Mukhopadhyay, A.S. Mahapatra, P.K. Chakrabarti, J. Magn. Magn. Mater. **329**, 133 (2013)
13. A. Jones, M.S. Islam, J. Phys. Chem. C **112**, 4455–4462 (2008)
14. P. Jain, S. Srivastava, N. Gupta, in *International Conference on Condensed Matter and Applied Physics*, Rajasthan (2015)
15. H. Wu, Z. Xia, X. Zhang, S. Huang, M. Wei, F. Yang, Y. Song, G. Xiao, Z. Ouyang, Z. Wang, Ceram. Int. **44**, 146–153 (2018)
16. L. Sun, H. Qin, K. Wang, M. Zhao, J. Hu, Mater. Chem. Phys. **125**, 305–308 (2011)
17. N. Karthikeyan, R. Ramesh Kumar, G. Jaiganesh, K. Sivakumar, Physica B **529**, 1–8 (2018)
18. A. Benali, S. Azizi, M. Bejar, E. Dhahri, M.F.P. Graça, Ceram. Int. **40**, 14367 (2014)
19. B. Ita, P. Murugavel, V. Ponnambalam, A.R. Raju, J. Chem. Sci. **115**, 519 (2003)
20. L.T. Sagdahl, M.-A. Einarsrud, T. Grande, J. Am. Ceram. Soc. **83**, 2318 (2000)
21. X.P. Dai, Q. Wu, R.J. Li, C.C. Yu, Z.P. Hao, J. Phys. Chem. B **110**, 25856 (2006)
22. A. Benali, A. Souissi, M. Bejar, E. Dhahri, M.F.P. Graça¸, M.A. Valente, Chem. Phys. Lett. **637**, 7 (2015)
23. M. Milanova, J. Zaharieva, R. Todorovska, D. Todorovsky, Thin Solid Films **562**, 43 (2014)
24. S. Nakayama, J. Mater. Sci. **36**, 5643 (2001)
25. F.B. Abdallah, A. Benali, M. Triki, E. Dhahri, M.P.F. Graca, M.A. Valente, Superlatt. Microstruct. **117**, 260 (2018)
26. H.M. Rietveld, J. Appl. Cryst. **2**, 65 (1969)
27. G. Aravind, M. Raghasudha, D. Ravinder, J. Magn. Magn. Mater. **378**, 278 (2015)
28. N.S. Goncalves, J.A. Carvalho, Z.M. Lima, J.M. Sasaki, Mater. Lett. **72**, 36 (2012)
29. K.S. Rao, B. Tilak, K. Ch, V. Rajulu, A. Swathi, H. Workineh, J. Alloys Compd. **509**, 7121 (2011)
30. M. Raghasudha, D. Ravinder, P. Veerasomaiah, Adv. Mater. Phys. Chem. **3**, 89 (2013)
31. S.T. Alone, K.M. Jadhav, Pramana, J. Phys. **70**, 173 (2008)
32. S. Thirumalairajan, K. Girija, I. Ganesh, D. Mangalaraj, C. Viswanathan, A. Balamurugan, N. Ponpandian, Chem. Eng. J. **209**, 420 (2012)
33. C. Sasikala, N. Durairaj, I. Baskaran, B. Sathyaseelan, M. Henini, E. Manikandan, J. Alloys Compd. **712**, 870 (2017)
34. Y. Janbutrach, S. Hunpratu, E. Swatsitang, Nanoscale Res. Lett. **9**, 498 (2014)
35. P. Tang, Y. Tong, H. Chen, F. Cao, G. Pan, Curr. Appl. Phys. **13**, 340 (2013)
36. P. Colomban, A. Slodczyk, Opt. Mater. **31**, 1759 (2009)
37. W. Chaabani, A. Melliti, A. Moadhen, M.A. Maaref, C. Testelin, A. Lemaître, M. Oueslati, Silicon **8**, 1 (2016)
38. I.S. Smirnova, Physica B **262**, 247 (1999)
39. M. Popa, L.V. Hong, M. Kakihana, Physica B **327**, 233 (2003)
40. S. Thirumalairajan, K. Girija, I. Ganesh, D. Mangalaraj, C. Viswanathan, N. Ponpandian, Cryst. Growth Des. **13**, 291 (2013)
41. L. Martín-Carrón, A. De Andrés, M.J. Martínez-Lope, M.T. Casais, J.A. Alonso, Phys. Rev. B **66**, 174303 (2002)
42. F.A. Mir, M. Ikrama, R. Kumar, J. Raman Spectrosc. **42**, 201 (2011)
43. S. Li, Y.H. Lin, B. Zhang, Y. Wang, C.W. Nan, J. Phys. C **114**, 2906 (2010)
44. M. Karmakar, B. Mondal, M. Pal, K. Mukherjee, Sens. Actuators B **190**, 627 (2014)
45. A.A. Al-Ghamdi, S. Al-Heniti, S.A. Khan, J. Lumin. **135**, 295 (2013)
46. A.O. Turky, M.M. Rashad, A.M. Hassan, E.M. Elnaggar, M. Bechelany, Phys. Chem. Chem. Phys. **19**, 6878 (2017)
47. M. Cesaria, A.P. Caricato, G. Leggieri, M. Martino, G. Maruccio, Thin Solid Films **545**, 592 (2013)
48. M.P. de Jong, V.A. Dediu, C. Taliani, W.R. Salaneck, J. Appl. Phys. **94**, 7292–7296 (2003)
49. K. Takenaka, Y. Sawaki, R. Shiozaki, S. Sugai, Phys. Rev. B **62**, 13864–13867 (2000)
50. F.M. Smits, Bell Syst. Tech. J. **37**, 711 (1958)